Quasiparticle Band Structure and Phonon-Induced Band Gap Renormalization of the Lead-Free Halide Double Perovskite Cs2InAgCl6

Viet-Anh Ha, George Volonakis, Hyungjun Lee, Marios Zacharias, Feliciano Giustino

Quasiparticle Band Structure and Phonon-induced Band Gap Renormalization of the Lead-free Halide Double Perovskite $Cs_2InAgCl_6$

Viet-Anh Ha,[†,‡] George Volonakis,[¶] Hyungjun Lee,[†,‡] Marios Zacharias,[§] and Feliciano Giustino[*,†,‡]

†*Oden Institute for Computational Engineering and Sciences, The University of Texas at Austin, 201 E. 24th Street, Austin, TX 78712, USA*

‡*Department of Physics, The University of Texas at Austin, Austin, TX 78712, USA*

¶*Université de Rennes, ENSCR, INSA Rennes, CNRS, ISCR-UMR 6226, F-35000 Rennes, France*

§*Department of Mechanical and Materials Science Engineering, Cyprus University of Technology, P.O. Box 50329, 3603 Limassol, Cyprus*

E-mail: fgiustino@oden.utexas.edu

Abstract

The lead-free halide double perovskite $Cs_2InAgCl_6$ was recently designed *in silico* and subsequently synthesized in the lab. This perovskite is a wide-gap semiconductor with a direct band gap, and exhibits extraordinary photoluminescence in the visible range upon Na doping. The light emission properties of $Cs_2InAgCl_6$ have successfully been exploited to fabricate stable single-emitter-based white light LEDs with near unity quantum efficiency. An intriguing puzzle in the photophysics of this compound is that the onset of optical absorption is around 3 eV, but the luminescence peak is found around 2 eV. As a first step toward elucidating this mismatch and clarifying the atomic scale mechanisms underpinning the observed luminescence, here we report a detailed investigation of the quasiparticle band structure of $Cs_2InAgCl_6$ as well as the phonon-induced renormalization of the band structure. We perform calculations of bang gaps and effective masses using the GW method, and we calculate the phonon-induced band structure renormalization using the special displacement method. We find that GW calculations are rather sensitive to the functional used in the density functional theory calculations, and that self-consistency on the eigenvalues is necessary to achieve quantitative agreement with experiments. Our most accurate band gap at room temperature is in the range 3.1-3.2 eV, and includes a phonon-induced gap renormalization of 0.2 eV. By computing the phonon-induced mass enhancement, we find that the electron carriers are in the weak polaronic coupling regime, while hole carriers are in the intermediate coupling regime as a result of the localized and directional nature of the Ag e_g $4d$ states at the valence band top.

1 TOC Graphic

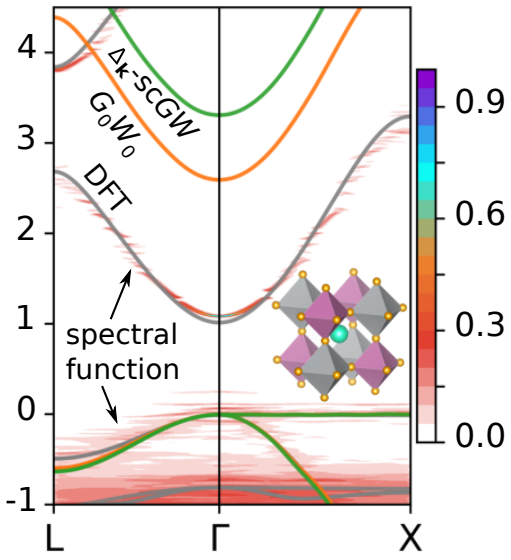

2 Introduction

The ABX_3 perovskite lattice is one of the most commonly occurring crystal structures.[1] Perovskites and perovskite-related materials find applications as ferroelectrics,[2,3] ferromagnets,[4] multiferroics,[5,6] semiconductors,[7–9] superconductors,[10,11] and solar absorbers.[12–17] Among the many families of perovskites, lead-based halide perovskites have attracted considerable interest owing to their extraordinary optoelectronic properties, leading to solar cells with energy conversion efficiencies as high as 25.5%.[17,18] Furthermore, the presence of a potentially toxic element in these compounds and their tendency to degrade in humid environments[19,20] prompted the search for alternative, lead-free materials with the perovskite structure.[21,22]

One class of lead-free perovskites that has gained significant attention are the ordered halide double perovskites (HDP) or 'elpasolites'.[21] The first HDPs with band gaps in the visible range, $Cs_2BiAgCl_6$ and $Cs_2BiAgBr_6$, have been designed and synthesized in early 2016.[23–25] Subsequent work along this direction led to the discovery of additional new HDPs such as $Cs_2SbAgCl_6$, $Cs_2SbAgBr_6$, $Cs_2InAgCl_6$, $Cs_2AgTlCl_6$, $Cs_2AgTlBr_6$, and even the oxide Ba_2AgIO_6.[26–31] Many of these new compounds have since been employed in a range of applications, including solar cells, photocatalysts, light emitters, and photodetectors.[32–45] Of these HDPs, $Cs_2InAgCl_6$[26] turned out to be an exceptionally efficient emitter of warm white light.[46]

At room temperature $Cs_2InAgCl_6$ crystallizes in a face-centered cubic lattice with space group $Fm\bar{3}m$. The unit cell contains 10 atoms arranged in two corner-sharing octahedra centered on the Ag and In cations, respectively, with the Cl anions at the vertices and the Cs cation in the cuboctahedral cages, as shown in Fig. 1. The first optical measurements on this compound were performed on powder samples, and revealed an absorption onset at 380 nm (3.26 eV) and a broad photoluminescence (PL) peak centered at 608 nm (2.04 eV) with full width at half maximum (FWHM) of 0.4 eV.[26] These observations were subsequently confirmed by UV-Vis spectra on single-crystal samples.[47] In Ref. 46 it was found that this PL signal can dramatically be enhanced by doping $Cs_2InAgCl_6$ with Na. This discovery enabled

the fabrication of single-emitter-based white-light LEDs with a record-high quantum yield of 86% and lifetimes up to 1000 hours.[46] Further work confirmed that Na and/or Bi doping lead to strong and broad PL,[46,48–53] thus establishing $Cs_2InAgCl_6$ as a new HDP with exceptional promise for LED applications.

Based on the large mismatch between the optical absorption onset (> 3 eV) and the PL peak ($\sim$2 eV), and the observation of photo-chromism, Ref. 26 tentatively attributed the PL signal to the formation of photo-induced defects. On the other hand, Ref. 46 proposed that the PL originates from the formation of self-trapped excitons driven by strong electron-phonon coupling in the form of Jahn-Teller distortions. A definitive assignment is further complicated by the fact that the magnitude of the band gap is not fully settled. For example, *ab initio* calculations using hybrid HSE or PBE0 functionals yield gaps ranging from 2.1 to 3.3 eV,[26] while GW calculations indicate gaps ranging from 3.1 to 3.3 eV.[46,54] All these previous calculations do not include the effect of electron-phonon coupling, which could significantly renormalize the band gap.[55–78] On the experimental front the optical gap is better understood, but quantitative differences remain. For example, UV-Vis spectra from different research groups yield optical gaps between 3.17 and 3.53 eV depending on sample morphology.[26,28,33,47,49,51,79–81]

In this work, as a first step toward elucidating the origin of the strong PL in $Cs_2InAgCl_6$ and related materials, we focus on the accurate determination of the band structure of this compound by employing GW calculations and including the electron-phonon renormalization of the bands via the special displacement method.[82,83] In particular, we carry out a thorough sensitivity analysis of GW quasiparticle band gaps in relation to the density functional theory (DFT) starting point and the use of self-consistency on the eigenvalues. We determine accurate band structures and effective masses by means of Wannier interpolation, and we calculate the electron-phonon renormalization of the band gap and effective masses using the special displacement method.

The manuscript is organized as follows: In Sec. 3 we briefly review the theoretical and

computational approach employed in this work, from the GW method to the special displacement method. The computational setup, including details on software and convergence tests, is described in Sec. 4. Section 5 presents our main results for the band gap, band structures, effective masses, and phonon-induced renormalization of the bands. In this section we also compare our results to experiments. In Sec. 6 we draw our conclusions and discuss the possible origin of the visible PL in $Cs_2InAgCl_6$.

3 Overview of methodology

3.1 *GW* calculations

The GW method[84–87] constitutes the most reliable parameter-free approach for computing quasiparticle band structures in weakly- to moderately-correlated solids. In this method, quasiparticle eigenvalues including nonlocal exchange and dynamical correlation are obtained by replacing the DFT exchange and correlation potential V_{xc} with the many-body self energy $\Sigma = GW$.[84] In this symbolic expression, G is the electron Green's function, and is evaluated using DFT Kohn-Sham wavefunctions and eigenvalues, and W is the screened Coulomb interaction, which is evaluated within the random-phase approximation (RPA) using once again DFT wavefunctions and eigenvalues. The quasiparticle energy $E_{n\mathbf{k}}$ is calculated perturbatively as $E_{n\mathbf{k}} = \varepsilon_{n\mathbf{k}} + Z_{n\mathbf{k}}\langle\psi_{n\mathbf{k}}|\Sigma(\varepsilon_{n\mathbf{k}}) - V_{xc}|\psi_{n\mathbf{k}}\rangle$, where $\varepsilon_{n\mathbf{k}}$ is the DFT eigenvalue corresponding to the electronic band n and wavevector $\mathbf{k}$, and $\psi_{n\mathbf{k}}$ is the associated wavefunction. $Z_{n\mathbf{k}}$ is the quasiparticle renormalization, and the self-energy is evaluated at the unperturbed DFT energy, $\Sigma(\varepsilon_{n\mathbf{k}})$.[84,87]

The above approach works best when the quasiparticle correction to DFT eigenvalues is relatively small. For large corrections, this method suffers from the sensitivity of the self-energy to the DFT band structure and wavefunctions.[88–93] In order to reduce this sensitivity, it is common to perform a few iterations where the eigenvalues used to calculate the self-energy at each iteration are taken from the result of the previous iteration.[84] This approach

has been used for a variety of systems, ranging from molecules to semiconductors.[94–99]

A simpler self-consistent procedure consists of updating a scissor correction instead of all individual eigenvalues.[100,101] The advantage of the self-consistent scissor is that the correction is well defined for all empty bands, and there is no need for extrapolations as in the case of eigenvalue-self-consistency. The scissor operator is simply defined as $\sum_{\mathbf{k}} \Delta_{\mathbf{k}} \hat{P}^{\mathrm{c}}_{\mathbf{k}}$, where $\hat{P}^{\mathrm{c}}_{\mathbf{k}}$ is the projector on the empty states with wavevector $\mathbf{k}$, and $\Delta_{\mathbf{k}}$ is a $\mathbf{k}$-dependent scissor correction. In the presence of a scissor correction, the quasiparticle eigenvalues are evaluated as $E_{n\mathbf{k}} = \varepsilon_{n\mathbf{k}} + Z_{n\mathbf{k}} \langle \psi_{n\mathbf{k}} | \Sigma(\varepsilon_{n\mathbf{k}}) - V_{xc} - \Delta_{\mathbf{k}} \hat{P}^{\mathrm{c}}_{\mathbf{k}} | \psi_{n\mathbf{k}} \rangle$. For completeness, in this work we also perform calculations using a $\mathbf{k}$-independent scissor correction evaluated at the direct gap. Self-consistent-scissor GW calculations proceed in the same way as for eigenvalue-self-consistency: the scissor correction determined at a given iteration is employed as a starting point for the evaluation of G and W in the next iteration, until convergence is achieved. For comparison, we also perform band structure calculations using the HSE functional, which has been very successful in calculations of extended solids.[102,103]

GW and HSE calculations are notoriously expensive. In order to calculate band structures along high-symmetry lines and evaluate the derivatives needed for the effective masses, we employ Wannier interpolation.[104,105] In particular, we perform GW and HSE calculations on coarse Brillouin zone grids, and we interpolate the eigenvalues using maximally localized Wannier functions.[106]

We evaluate effective masses by taking second order derivatives of the eigenvalues via finite differences. In particular, we evaluate $1/m_{\alpha\beta} = \hbar^{-2} \partial^2 E_{n\mathbf{k}} / \partial k_\alpha \partial k_\beta$, where $\hbar$ is Planck's constant and α, β indicate Cartesian directions. We evaluate the masses using second-order mixed finite difference formulas; the values reported below are the eigenvalues of the effective mass tensors.

3.2 Special displacement calculations

To investigate the phonon-induced renormalization of the band structure of $Cs_2InAgCl_6$, we employ the special displacement method.[82,83] This method consists of performing a band structure calculation for a supercell where the atoms have been displaced from their equilibrium sites. The displacements are chosen so as to reproduce the thermal mean square displacements including quantum zero-point fluctuations within a single supercell calculation. The special set of displacements is referred to as the ZG (Zacharias-Giustino) displacement, and it is understood as the mean-value point of the multi-dimensional Williams-Lax integral.[83] This method was successfully employed to calculate temperature-dependent band structure renormalization in numerous semiconductors and insulators.[107–111] The ZG displacement is given by:

$$\Delta\tau_{\kappa\alpha}(\mathbf{R}) = \sum_{\mathbf{q},\nu} S_{\mathbf{q}\nu} \left[\frac{\hbar}{2NM_\kappa\omega_{\mathbf{q}\nu}}(2n_{\mathbf{q}\nu,T}+1)\right]^{\frac{1}{2}} 2\,\mathrm{Re}\left[e^{i\mathbf{q}\cdot\mathbf{R}} e_{\kappa\alpha,\nu}(\mathbf{q})\right] , \tag{1}$$

where $\Delta\tau_{\kappa\alpha}(\mathbf{R})$ indicates the displacement of the atom κ with mass M_κ in the unit cell with lattice vector $\mathbf{R}$, and N is the number of unit cells in the supercell. $e_{\kappa\alpha,\nu}(\mathbf{q})$ is the polarization vector of the phonon (normalized within the unit cell) with wavevector $\mathbf{q}$, branch index ν, frequency $\omega_{\mathbf{q}\nu}$, and Bose-Einstein occupation $n_{\mathbf{q}\nu,T}$ at the temperature T. The quantities $S_{\mathbf{q}\nu}$ are signs (±1) determined so as to yield the correct quantum canonical average of the displacements in the thermodynamic limit of an infinitely-extended supercell. The summation in Eq. (1) is restricted to $\mathbf{q}$-vectors that are neither time-reversal invariant nor time-reversal partner of another vector in the sum. The phonon frequencies and eigenvectors needed in Eq. (1) are obtained via density-functional perturbation theory.[112]

To obtain the electron spectral function in the presence of electron-phonon interactions, we unfold the band structure calculated for the supercell with the ZG displacement.[83,113] The resulting bands include electron-phonon renormalization to second order in the atomic displacements as in the Allen-Heine theory,[114] as well as all higher orders of electron-phonon

coupling and off-diagonal Debye-Waller corrections.[55,115]

4 Computational setup and convergence tests

All DFT calculations were performed using planewaves and pseudopotentials, as implemented in the Quantum ESPRESSO suite.[116] We considered three exchange and correlation functionals: LDA,[117] PBE,[118] and PBEsol.[119] We employed optimized norm-conserving Vanderbilt pseudo-potentials (ONCVPSP)[120] from the PseudoDojo library.[121] The valence configurations for Cs, Ag, and Cl are $5s^2p^66s^1$, $4s^2p^6d^{10}5s^1$, and $3s^2p^5$, respectively. For In the library offers pseudopotentials with semicore states, $4s^2p^6d^{10}5s^2p^1$, and without semicore states, $4d^{10}5s^2p^1$. We tested both options to investigate the sensitivity of GW calculations to semicore electrons. Following the PseudoDojo recommendations we used a stringent kinetic energy cutoff of 100 Ry for all calculations. To confirm that this cutoff is sufficient for $Cs_2InAgCl_6$, we also tested 120, 140, and 160 Ry, and we found that 100 Ry yields lattice parameters and GW shifts within 10^{-4} Å and 1 meV of the most accurate calculation at 160 Ry.

Structural optimization was carried out using very stringent convergent criteria for the total energy (10^{-12} Ry), forces (10^{-6} Ry/bohr), and pressure (10^{-3} kbar). The optimized lattice constants are 10.19 Å, 10.66 Å, and 10.38 Å for the LDA, PBE, and PBEsol functional, respectively. As expected, the PBEsol functional produces the lattice constant closest to the experimental value of 10.47 Å.[26] Complete data about structural optimization is reported in Table 1.

All GW calculations were performed using the Yambo code[122,123] in conjunction with Quantum ESPRESSO.[116] We employed the Godby-Needs plasmon-pole model,[124] and set the plasmon energy to 21 eV based on calculations of the energy-loss function. In Fig. 2 we show our convergence tests for the kinetic energy cutoff of the dielectric matrix and the energy window used for the Green's function (or equivalently the number of empty

states). We considered cutoffs between 4 and 12 Ry for the dielectric matrix, and between 15 and 90 eV for the Green's function (100 to 650 bands). In this test we employed an $8 \times 8 \times 8$ Brillouin zone grid. Fig. 2 shows that using 10 Ry for the dielectric matrix and 600 bands is sufficient to obtain a band gap converged to within 10 meV. Using these converged parameters, we tested the sensitivity to the Brillouin zone sampling. To this end we repeated the calculations using uniform grids with 6^3 to 12^3 points, and found that the gap changes by 7 meV at most. Therefore a $6 \times 6 \times 6$ grid is already enough for our purposes. All subsequent calculations have been performed using $10 \times 10 \times 10$ grids. For eigenvalue-self-consistent GW calculations, we calculated the quasiparticle shifts for 14 valence bands and 14 conduction bands, and interpolated the corrections for the other bands.

Below we report GW calculations performed using the three exchange and correlation functionals LDA, PBE, and PBEsol. The band structures, gaps, and effective masses reported below were obtained using the optimized lattice parameter for each functional, unless otherwise stated. We also tested the effect of spin-orbit coupling by using fully-relativistic ONCVPSP pseudopotentials, but we found that it does not affect band structures in any significant way, in agreement with previous work.[28,125] Based on these results, we performed GW calculations without spin-orbit coupling.

HSE calculations were carried out starting from the PBE-optimized structure and a $10 \times 10 \times 10$ Brillouin zone grid, using the adaptively compressed exchange operator implemented in Quantum ESPRESSO.[126]

To facilitate Wannier interpolation, we excluded the first 27 bands which form a composite manifold below the valence bands for calculations in the presence of In semicore states (23 bands otherwise). This leaves 30 bands for Wannier interpolation. All calculations of Wannier functions were performed using the Wannier90 code.[127–129]

Effective masses were evaluated by finite differences using a step size of 10^{-3} Å^{-1} in reciprocal space, which guarantees an accuracy of 10^{-2} m_0, with m_0 being the free electron mass.

Phonon dispersion relations and eigenmodes were calculated using density-functional perturbation theory as implemented in the PHonon code of Quantum ESPRESSO.[116] For these calculations we used the PBE functional. The supercells with ZG displacements were obtained using the ZG.x code released with the EPW package.[83,130] We constructed special displacements in $3\times3\times3$, $4\times4\times4$, and $5\times5\times5$ supercells, containing up to 1250 atoms. To lower the computational cost of these calculations, we used a reduced planewaves cutoff of 76 Ry, as suggested by the PseudoDojo library.[121] We checked that band structure computed with 76 or 100 Ry cutoffs are pratically indistinguishable. The band gap red-shifts at 300 K obtained from $3 \times 3 \times 3$, $4 \times 4 \times 4$, and $5 \times 5 \times 5$ supercells are 123 meV, 187 meV, and 165 meV, respectively [c.f. inset of Fig. 8(a)]. Based on these calculations, we expect the converged value of the electron-phonon renormalization to fall in the interval 176±11 meV. To reduce the cost of these calculations, we analyze band structures for the $4\times4\times4$ supercell, which yields a renormalization within 10% of our most converged value.

5 Results and discussion

5.1 Quasiparticle band gap and effective masses

The band structures of $Cs_2InAgCl_6$ calculated using DFT, GW, and HSE are shown in Fig. 3. This compound exhibits a direct gap at the Γ point. The conduction band minimum (CBM) originates from In/Ag-5s and Cl-3p states, while the valence band maximum (VBM) results from the hybridization of Ag e_g states ($4d_{x^2-y^2}$ and $4d_{z^2}$) with Cl-3p states. The flat band visible along the Γ-X line at the top of the valence bands originates from the hybridization of $4d_{x^2-y^2}$ states of Ag with the Cl-3$p_{x,y}$ states, leading to a two-dimensional wavefunction confined within the xy plane.[26]

An example of the iterative procedure for self-consistent GW calculations is given in Fig. 4. This plot shows how, upon performing self consistency on the eigenvalues starting from PBE, the band gap increases from 2.6 eV to 3.4 eV after five iterations. Similar trends

are observed when considering self-consistent scissor corrections, with the converged value being only slightly smaller at 3.3 eV. The monotonic increase of the band gap upon self-consistency is understood as the result of the improved RPA screening resulting from the wider band gap obtained at each iteration. In comparison, the one-shot (G_0W_0) gap is underestimated because the initial PBE gap is extremely small (1 eV) as compared to the final quasiparticle gap (3.4 eV).

In Table 2 we report a comprehensive dataset of band gaps computed using various self-consistency schemes for GW, starting from three DFT functionals, with or without In semicore states, and using the optimized or experimental lattice parameters. Key data is also reported in Fig. 5. As expected, semicore states play an important role in the calculated GW gaps, causing a blueshift of up to 0.4 eV as compared to calculation without semicore states [Table 2(a)]. This is understood in terms of the exchange self-energy being sensitive to the overlap between semicore states and band edge states.[131–133] Among the functionals employed, the DFT band gap is smallest for LDA and largest for PBE. This trend is reflected in the corresponding GW band gaps. The same trends are observed when performing all calculations using the experimental lattice constant, as shown in Table 2(b). The choice of using optimized or experimental lattice constant brings only a small change in the gap, in the range of 0.1 eV, as it can be seen in Table 2(c). Furthermore, the use of eigenvalue-self-consistency or scissor-self-consistency is found to reduce the dependence of the GW band gap on the DFT starting point, approximately halving the differences between LDA, PBE, and PBEsol calculations. In comparison, HSE calculations yield too small a band gap, in the same range as the result of one-shot G_0W_0 calculations (Table 2).

In Fig. 5 we compare our calculations with measured absorption onsets in UV-Vis spectra. Experimental data is from powder samples,[26] single crystalline samples,[33,47] films,[28,81] and nanocrystals.[49,51,79,80] Even after excluding nanocrystals which might be affected by quantum confinement, there is a significant scatter between reported gaps, from 3.2 eV[33] to 3.53 eV.[28,81] These values are shown in pink in Fig. 5, and the experimental range is

indicated by a gray horizontal stripe.

A comparison between our calculations and experiments indicates that eigenvalue- or scissor-self-consistent GW calculations starting from the PBE functional lie well within the experimental range, while the other options explored here tend to slightly underestimate the experimental values. We should also keep in mind that the measured optical gaps might include non-negligible renormalization from excitonic effects and electron-phonon interactions. These effects will further lower the theoretical band gaps in Fig. 5. In particular, in Sec. 5.2 we will show that the electron-phonon interactions reduce the band gap by as much as ~ 0.2 eV at room temperature.

Fig. 3(c) shows how quasiparticle corrections modify the curvature of the bands near the band extrema. To quantify this effect, we report in Fig. 6 the effective masses calculated at various levels of theory. Unlike for the band gaps, we find that the effective mass renormalization is not very sensitive to the DFT starting point for the GW calculations, and that HSE masses are similar to GW masses.

The band edges of $Cs_2InAgCl_6$ can be described via an electron mass, a light hole mass, and a heavy hole mass, as it can be seen in Fig. 3(c). We find that both electron and hole effective mass tensors are isotropic, therefore in Fig. 6 we report only the isotropic average. Taking $\Delta_{\mathbf{k}}$-scGW calculations with PBE starting point as a reference, we find that the electron mass increases by 15% from 0.27 m_0 (PBE) to 0.31 m_0 (GW), while the light hole mass decreases by 20% from 0.36 m_0 to 0.30 m_0, and the heavy hole mass decreases by 17% from 0.90 m_0 to 0.77 m_0. We note that the determination of the heavy hole mass is less reliable owing to the non-dispersive nature of the top of the valence bands along the Γ-X direction.

To the best of our knowledge, no measurements of the effective masses in $Cs_2InAgCl_6$ are available. However, given that GW calculations of quasiparticle effective masses in the related halide $CH_3NH_3PbI_3$ closely reproduce experimental effective masses obtained from magnetic measurements of exciton binding energies,[134] we expect our calculations to carry

reasonable predictive power.

The much heavier carrier effective masses of $Cs_2InAgCl_6$ as compared to the prototypical halide perovskite $CH_3NH_3PbI_3$ ($\sim 0.1\,m_0$, Ref. [134]) suggest that this compound will exhibit poor transport properties. Indeed, the calculated carrier mobility of the related double perovskite $Cs_2BiAgCl_6$, which exhibits effective masses similar to $Cs_2InAgCl_6$, lies in the range 6-11 cm^2/Vs depending on direction,[135] therefore for $Cs_2InAgCl_6$ we can expect mobilities within this same range. This tentative estimate is in line with both experimental measurements of the carrier mobility in $Cs_2InAgCl_6$, yielding 2.3-3.3 cm^2/Vs,[33] and theoretical estimates based on a Fröhlich polaron model, yielding 2.34 cm^2/Vs.[79] Clearly further work will be needed to clarify the conduction mechanisms in $Cs_2InAgCl_6$ and related materials, and to understand how the transport properties of this compound can be improved via doping.[79]

5.2 Electron-phonon coupling

Figure 7 shows the calculated phonon dispersion relations of $Cs_2InAgCl_6$, as well as the phonon density of states (DOS) projected onto Cs, Ag/In, and Cl displacements. The lack of soft modes confirms that $Cs_2InAgCl_6$ is dynamically stable in the $Fm\bar{3}m$ structure. We can see three main groups of vibrations: a low-energy group around 5-10 meV, which is dominated by the vibrations of Cs and Ag, an intermediate-energy group of modes around 15 meV, associated with the bending motion of the Ag-Cl/In-Cl bonds, and high-energy modes in the range 25-30 meV associated with Ag-Cl and In-Cl stretching vibrations. The phonon dispersions and the mode assignment are similar to the related double perovskite $Cs_2BiAgCl_6$.[135]

In Fig. 8 we show the momentum-resolved spectral function and the electronic DOS of $Cs_2InAgCl_6$ including electron-phonon interactions at 300 K, as obtained via the special displacement method.[83] Electron-phonon couplings are seen to shift and broaden the non-interacting DFT bands, which are also shown in Fig. 8 as gray lines for comparison.

Phonon-induced renormalization is most pronounced for the valence bands. Indeed, the VBM acquires a finite linewidth of 143 meV and blueshifts by 255 meV. In contrast, the CBM acquires a finite linewidth of 9 meV, and blueshifts by 68 meV. To rationalize this significant difference between VBM and CBM, in Fig. 9 we show the electron density around the metal-halide octahedra, for both the ground state structure and the perturbed ZG structure at 300 K, evaluated at the Γ point. From this comparison we see that the diffuse and isotropic nature of the Ag/In-5s states makes the CBM wavefunction relatively insensitive to lattice fluctuations. On the other hand, the more localized and directional nature of the Ag e_{g} states ($4d_{x^2-y^2}$ and $4d_{z^2}$) makes the VBM wavefunction more responsive to a breaking of octahedral symmetry.

The uneven temperature shift of VBM and CBM leads to a band gap renormalization of 187 meV at 300 K. Combined with our self-consistent GW calculations in Table 2 (starting from PBE), this result implies that our most accurate theoretical gap of $Cs_2InAgCl_6$, including both many-body electron-electron and electron-phonon interactions, should be in the range 3.07-3.19 eV. It is worth noting that the electron-phonon coupling evaluated at the PBE level is expected to be slightly too weak (by a few tens of percent) as a result of the band gap underestimation.[64] Therefore, our calculations of the band gap renormalization likely constitute a lower bound to the true effect, and our final band gap range is probably overestimated by a few tens of meV.

Given that the conduction band near the CBM is relatively sharp [see Fig. 8(a)], it is possible to extract the renormalized electron effective mass from the spectral function using a simple parabolic fit. This procedure yields the effective mass 0.33 m_0 at 300 K. Since the bare mass is 0.27 m_0, we conclude that phonons induce a mass enhancement of 22 %. Assuming that the most significant contribution arises from longitudinal optical phonons as for the related $CH_3NH_3PbI_3$ and $Cs_2AgBiCl_6$,[135,136] we can use the mass renormalization to extract an approximate polaron coupling constant α.[137] The mass enhancement in Feynman's model[138] is given by $1+\alpha/6+0.025\alpha^2$, yielding a coupling constant $\alpha = 1.1$ for electrons in

$Cs_2InAgCl_6$. This value indicates a weak polaron coupling regime for the electrons. We also estimate the size of polaronic carriers using Feynman's expression, $r_p = (3.4\,\hbar/m^*\,\alpha\,\omega)^{1/2}$.[139] Using $\hbar\omega = 32.7$ meV from Fig. 7 and $m^* = 0.27\,m_0$, we find $r_p = 52$ Å, indicating large electron polarons. This analysis suggests that electron carriers in $Cs_2InAgCl_6$ undergo standard diffusive transport. A similar parabolic fit for the light hole carriers (along the Γ-L direction) yields a much more pronounced mass enhancement, from $0.36\,m_0$ to $1.2\,m_0$, therefore in this case we have $\alpha = 6.9$ and $r_p = 18$ Å. As expected, in this simple model the holes form intermediate polarons, hence thermal activation may play an important role in hole transport.

6 Conclusions

In this work we reported a detailed investigation of the quasiparticle band structure and electron-phonon couplings in the lead-free halide double perovskite $Cs_2InAgCl_6$. We performed a thorough sensitivity analysis of the GW quasiparticle corrections by considering several DFT exchange and correlation functionals as starting point, and several strategies for self-consistency. In addition, we computed the band gap renormalization arising from electron-phonon interactions at room temperature via the special displacement method. Upon including both electron-electron and electron-phonon interactions, our most accurate estimate for the band gap is 3.07-3.19 eV. These values are well within the experimental band gap range as determined via UV-Vis absorption spectroscopy. In comparison, we found that both the one-shot G_0W_0 and HSE band gaps underestimate the band gap by as much as an eV, hence they do not provide a reliable description of the band structure of $Cs_2InAgCl_6$. The present study indicates that the luminescence of this compound around 2 eV is not related to band-to-band recombination, which occurs at a much higher energy. Remaining options to explain the observed PL are the formation of strongly bound polarons, defect-induced emission, and self-trapped excitons. Regarding polarons, our simplified analysis based on

Feynman's model indicates that electron carriers are in the large polaron coupling regime, while hole carriers are moderately coupled to phonons due to the $d_{x^2-y^2}$ and d_{z^2} character of the VBM. It is likely that hole carriers in this compound form intermediate polarons, although a precise determination of the polaron formation energies will require a separate, detailed investigation. In summary, this work establishes clear guidelines for future *ab initio* calculations of the electronic and optical properties of $Cs_2InAgCl_6$, and provides a firm basis for quantitative studies of the photophysics of this promising light-emitting material.

7 Acknowledgments

This work is supported by the Robert A. Welch Foundation under award number F-1990-20190330 (V.H., calculations and data analysis) and the Computational Materials Sciences Program funded by the U.S. Department of Energy, Office of Science, Basic Energy Sciences, under Award No. DE-SC0020129 (H.L., Wannier functions, and F.G., project supervision). G.V. acknowledges the Chaire de Recherche Rennes Métropole. The authors acknowledge the Texas Advanced Computing Center (TACC) at The University of Texas at Austin for providing HPC resources, including the Lonestar5 system and Frontera under LRAC award 2007638, that have contributed to the research results reported within this paper. URL: http://www.tacc.utexas.edu. This research also used resources of the National Energy Research Scientific Computing Center, a DOE Office of Science User Facility supported by the Office of Science of the U.S. Department of Energy under Contract No. DE-AC02-05CH11231.

Table 1: Optimized structure of cubic $Cs_2InAgCl_6$ with space group $Fm\bar{3}m$. We report the Wyckoff site and fractional coordinates of each atom in the primitive cell obtained using the LDA, PBE, and PBEsol functionals, as well as the bond lengths and lattice constants. For reference, the measured lattice constant is 10.47 Å.[26] Only data obtained by including In semicore states are reported; the bond lengths and lattice constants calculated without semicore states are within 0.05% (0.01 Å) of the values reported below.

							LDA	PBE	PBEsol
Cs	2c	$(1/4, 1/4, 1/4)$	Cl	6e	(x, y, x)	x	0.754	0.759	0.756
Cs	2c	$(3/4, 3/4, 3/4)$	Cl	6e	(y, x, y)	y	0.246	0.241	0.244
In	1a	$(0, 0, 0)$	Cl	6e	(x, y, y)	In-Cl (Å)	2.5043	2.5705	2.5327
Ag	1b	$(1/2, 1/2, 1/2)$	Cl	6e	(y, x, x)	Ag-Cl (Å)	2.5927	2.7609	2.6592
			Cl	6e	(x, x, y)	a (Å)	10.1933	10.6629	10.3838
			Cl	6e	(y, y, x)				

Table 2: Bandgap of $Cs_2InAgCl_6$ calculated using DFT, GW, and HSE. (a) Calculations perfomed using the optimized structures for each functional, as described in Table 1. (b) Calculations performed using the experimental lattice constant and the fractional coordinates reported in Table 1 for each functional. (c) Difference between the values obtained in (b) and in (a). In all cases we report results including or excluding In semicore states. The labels on the leftmost column indicate eigenvalue-self-consistent GW (ev-scGW), self-consistent scissor GW with a **k**-independent scissor (Δ_Γ-scGW), and self-consistent scissor GW with a **k**-dependent scissor ($\Delta_{\mathbf{k}}$-scGW). HSE calculations were performed using the structure optimized via the PBE functional.

		LDA		PBE		PBEsol	
		no semicore	semicore	no semicore	semicore	no semicore	semicore
(a)	DFT	0.60	0.60	1.02	1.03	0.78	0.79
	G_0W_0	2.03	2.39	2.30	2.60	2.12	2.45
	ev-scGW	2.69	3.12	3.02	3.38	2.81	3.20
	Δ_Γ-scGW	2.58	3.07	2.84	3.26	2.67	3.12
	$\Delta_{\mathbf{k}}$-scGW	2.59	3.06	2.91	3.31	2.70	3.14
	HSE	-	-	2.25	2.46	-	-
(b)	DFT	0.50	0.50	1.08	1.09	0.75	0.76
	G_0W_0	1.90	2.23	2.37	2.68	2.09	2.41
	ev-scGW	2.59	3.00	3.06	3.44	2.78	3.17
	Δ_Γ-scGW	2.47	2.94	2.90	3.32	2.64	3.08
	$\Delta_{\mathbf{k}}$-scGW	2.48	2.93	2.96	3.37	2.67	3.10
	HSE	-	-	2.33	2.55	-	-
(c)	DFT	(-0.10)	(-0.10)	(0.06)	(0.06)	(-0.03)	(-0.03)
	G_0W_0	(-0.13)	(-0.16)	(0.07)	(0.08)	(-0.03)	(-0.04)
	ev-scGW	(-0.10)	(-0.12)	(0.04)	(0.06)	(-0.03)	(-0.03)
	Δ_Γ-scGW	(-0.11)	(-0.13)	(0.06)	(0.06)	(-0.03)	(-0.04)
	$\Delta_{\mathbf{k}}$-scGW	(-0.11)	(-0.13)	(0.05)	(0.06)	(-0.03)	(-0.04)
	HSE	-	-	(0.08)	(0.09)	-	-

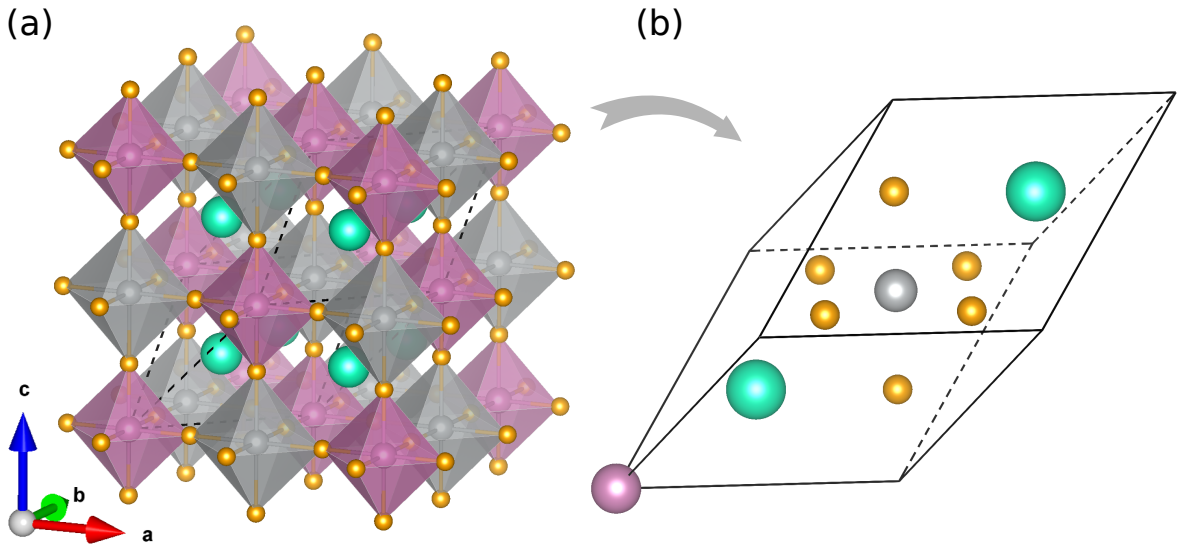

Figure 1: Ball-and-stick model of (a) conventional cell, and (b) primitive unit cell of $Cs_2InAgCl_6$. The color code is as follows, Cs: cyan; In: purple, Ag: grey, and Cl: orange. The structure belongs to the $Fm\bar{3}m$ space group, and the experimental lattice parameter is 10.47 Å.[26] The PBEsol Ag-Cl and In-Cl bond lengths are 2.659 Å and 2.533 Å, respectively, see Table 1.

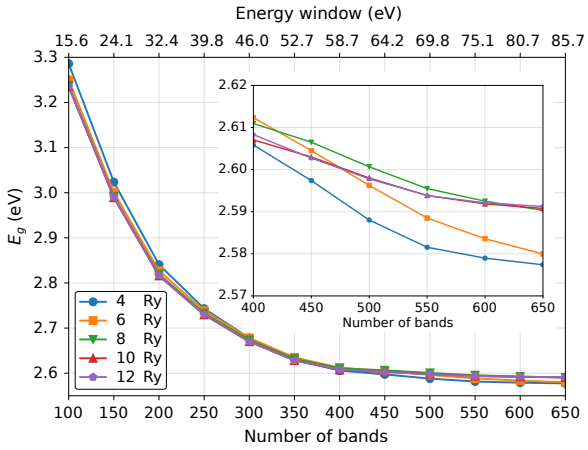

Figure 2: Convergence test for the GW calculations. The one-shot GW band gap of $Cs_2InAgCl_6$ is calculated starting from PBE, as a function of the number of bands (energy window) and of the kinetic energy cutoff for the dielectric matrix. The energy window is referred to the top of the valence bands. The inset is a zoom near the region where convergence is achieved.

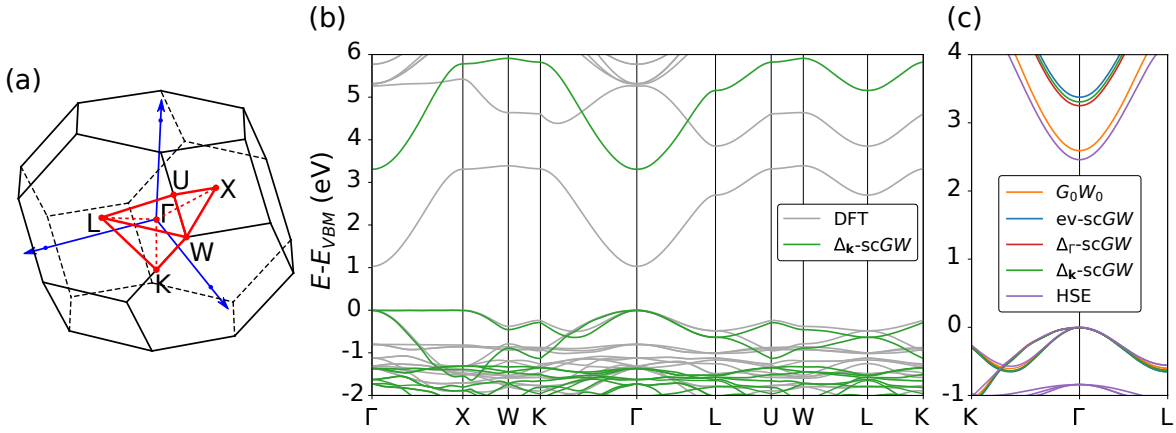

Figure 3: Band structure of $Cs_2InAgCl_6$ computed at various levels of theory. (a) Brillouin zone of $Cs_2InAgCl_6$ and high-symmetry points used in the band structure plots. (b) Comparison between the PBE band structure (gray) and the $\Delta_{\mathbf{k}}$-scGW band structure starting from PBE (green). The GW bands are obtained with the PBE functional and ONCVPSP pseudopotentials including In semicore states. (c) Comparison between the GW band structures obtained using G_0W_0 (orange), ev-scGW (blue), Δ_Γ-scGW (red), $\Delta_{\mathbf{k}}$-scGW (green) and HSE (purple) near the band edges.

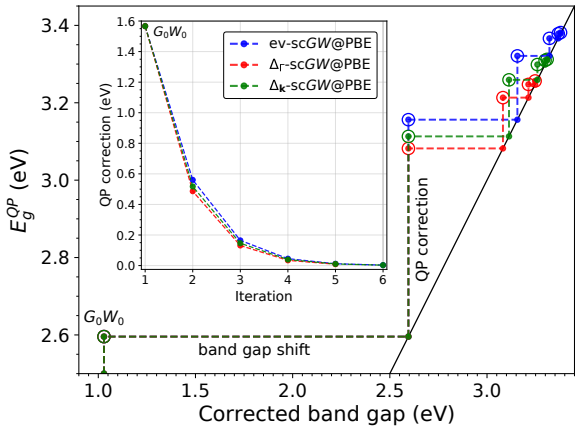

Figure 4: Convergence of eigenvalue-self-consistent (ev-scGW, blue) and scissor-self-consistent (Δ_Γ-scGW, red, and $\Delta_\mathbf{k}$-scGW, green) calculations of the band gap of $Cs_2InAgCl_6$. At each iteration, the starting band gap on the horizontal axis is obtained from the GW gap at the previous iteration on the vertical axis. The inset shows the change in band gap between successive iterations.

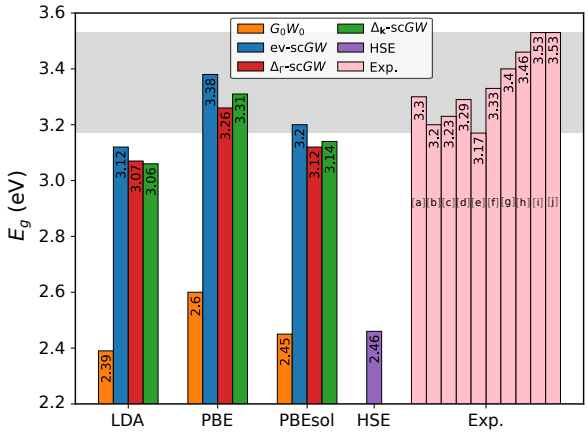

Figure 5: GW band gaps calculated starting from various DFT functionals. We report the one-shot G_0W_0 gaps (orange), the eigenvalue-self-consistent GW gaps (blue), and the scissor-self-consistent GW gaps (Δ_Γ-scGW, red; $\Delta_\mathbf{k}$-scGW, green). For comparison we also report the HSE gap (purple), and the experimental data (pink). All GW calculations include In semicore states. The experimental references are as follows: a) Powder samples, Ref. 26, b) Single crystal, Ref. 33, c) Single crystal, Ref. 47, d) Single crystal, Ref. 28, e) Nanocrystal, Ref. 79, f) Nanocrystal, Ref. 80, g) Nanocrystal, Ref. 49, h) Nanocrystal, Ref. 51, i) Film, Ref. 28, j) Film, Ref. 81.

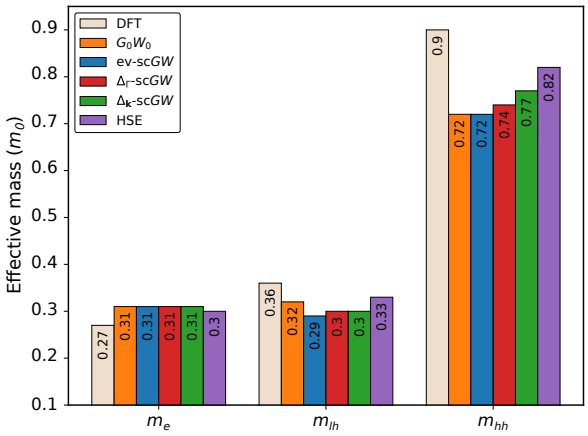

Figure 6: Calculated quasiparticle effective masses of $Cs_2InAgCl_6$. We provide the electron mass (m_e), light hole mass (m_{lh}), and heavy hole mass (m_{hh}). All calculations employ the PBE functional as a starting point. The acronyms are the same as in Fig. 5.

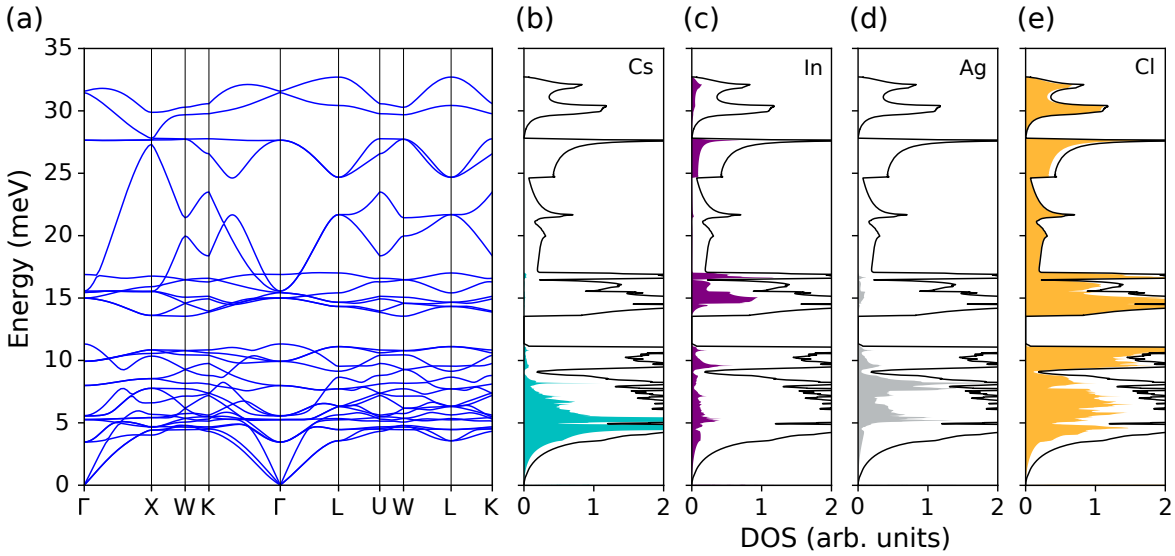

Figure 7: (a) Phonon dispersion relations of $Cs_2InAgCl_6$, calculated using DFT/PBE. (b) Total vibrational DOS (black line) and DOS projected on the displacements of Cs (cyan, filled). (c) Total DOS and DOS projected on the displacements of In (purple, filled). (d) Total DOS and DOS projected on the displacements of Ag (grey, filled). (e) Total DOS and DOS projected on the displacements of Cl (orange, filled).

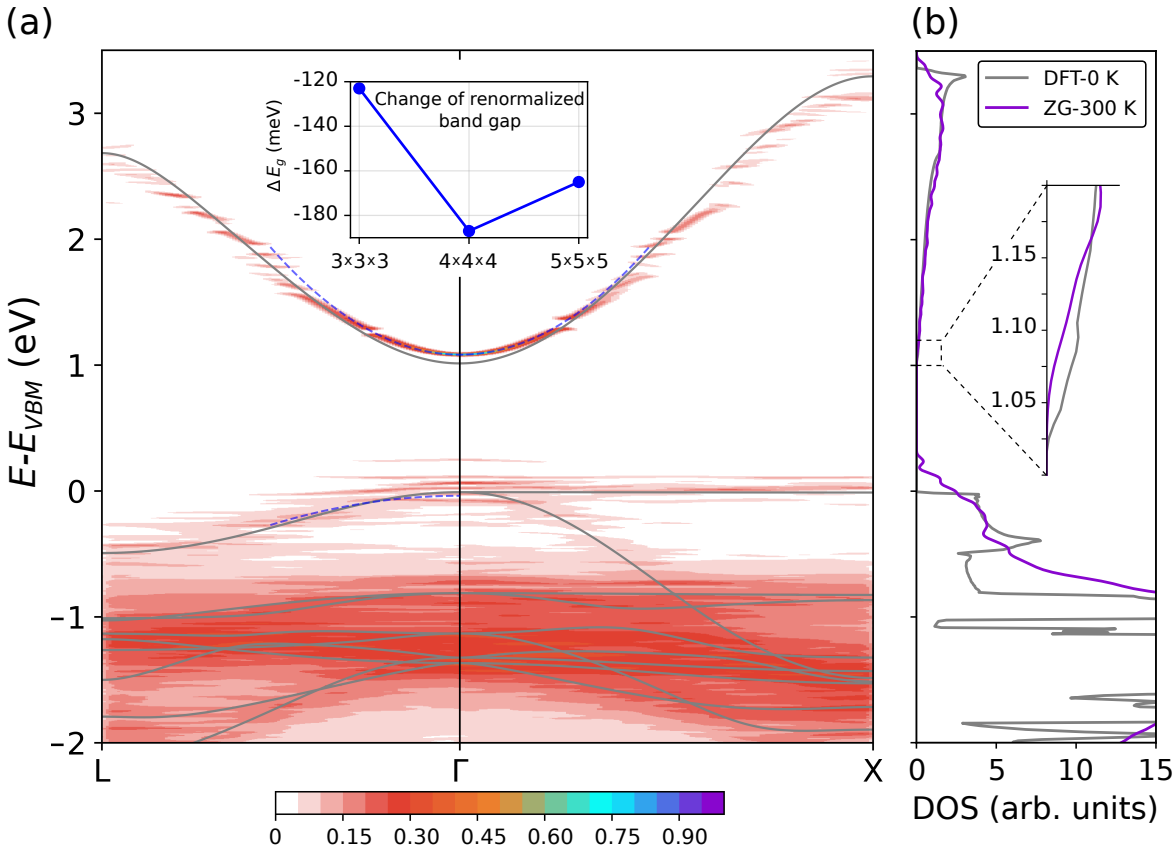

Figure 8: (a) Electron spectral function of $Cs_2InAgCl_6$ including electron-phonon interactions, evaluated at 300 K using the special displacement method ($4 \times 4 \times 4$ supercell, PBE). The grey solid lines indicate the unperturbed DFT band structure. The blue dashed lines indicate the parabolic fits used to determine the renormalized effective masses. Inset: Convergence of the renormalized band gap with supercell size. (b) Electronic DOS corresponding to the spectral function in (a). The violet line includes electron-phonon interactions, the grey line is the unperturbed DFT DOS.

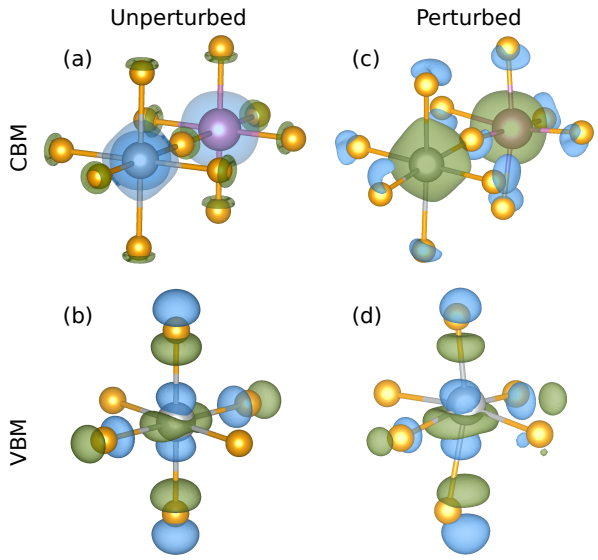

Figure 9: Wavefunction isosurfaces of the VBM and CBM of $Cs_2InAgCl_6$ in the unperturbed structure and after introducing thermal displacements. (a),(c) Close-up view of the CBM wavefunction (Γ point) without/with thermal displacements, respectively. (b),(d) Same as above, but for the VBM. Blue/green indicates a positive/negative sign, respectively. The VBM is mainly derived from Ag-4d/Cl-3p states, thus, only the $AgCl_6$ octahedron is shown.

References

(1) Filip, M. R.; Giustino, F. The geometric blueprint of perovskites. *Proc. Natl. Acad. Sci.* **2018**, *115*, 5397–5402.

(2) Benedek, N. A.; Fennie, C. J. Why Are There So Few Perovskite Ferroelectrics? *J. Phys. Chem. C* **2013**, *117*, 13339–13349.

(3) Paillard, C.; Bai, X.; Infante, I. C.; Guennou, M.; Geneste, G.; Alexe, M.; Kreisel, J.; Dkhil, B. Photovoltaics with Ferroelectrics: Current Status and Beyond. *Adv. Mater.* **2016**, *28*, 5153–5168.

(4) Loudon, J. C.; Mathur, N. D.; Midgley, P. A. Charge-ordered ferromagnetic phase in $La_{0.5}Ca_{0.5}MnO_3$. *Nature* **2002**, *420*, 797–800.

(5) Tokunaga, Y.; Furukawa, N.; Sakai, H.; Taguchi, Y.; Arima, T.-h.; Tokura, Y. Composite domain walls in a multiferroic perovskite ferrite. *Nat. Mater.* **2009**, *8*, 558–562.

(6) Mundy, J. A.; Brooks, C. M.; Holtz, M. E.; Moyer, J. A.; Das, H.; Rébola, A. F.; Heron, J. T.; Clarkson, J. D.; Disseler, S. M.; Liu, Z. et al. Atomically engineered ferroic layers yield a room-temperature magnetoelectric multiferroic. *Nature* **2016**, *537*, 523–527.

(7) Xing, G.; Mathews, N.; Sun, S.; Lim, S. S.; Lam, Y. M.; Gratzel, M.; Mhaisalkar, S.; Sum, T. C. Long-Range Balanced Electron- and Hole-Transport Lengths in Organic-Inorganic $CH_3NH_3PbI_3$. *Science* **2013**, *342*, 344–347.

(8) Lin, Y.-H.; Pattanasattayavong, P.; Anthopoulos, T. D. Metal-Halide Perovskite Transistors for Printed Electronics: Challenges and Opportunities. *Adv. Mater.* **2017**, *29*, 1702838.

(9) Gedda, M.; Yengel, E.; Faber, H.; Paulus, F.; Kreß, J. A.; Tang, M.-C.; Zhang, S.; Hacker, C. A.; Kumar, P.; Naphade, D. R. et al. Ruddlesden–Popper-Phase Hybrid Halide Perovskite/Small-Molecule Organic Blend Memory Transistors. *Adv. Mater.* **2021**, *33*, 2003137.

(10) Bednorz, J. G.; Müller, K. A. Possible high T_c superconductivity in the Ba-La-Cu-O system. *Z für Phys. B Condensed Matter* **1986**, *64*, 189–193.

(11) Murphy, D. W.; Sunshine, S.; van Dover, R. B.; Cava, R. J.; Batlogg, B.; Zahurak, S. M.; Schneemeyer, L. F. New superconducting cuprate perovskites. *Phys. Rev. Lett.* **1987**, *58*, 1888–1890.

(12) Lee, M. M.; Teuscher, J.; Miyasaka, T.; Murakami, T. N.; Snaith, H. J. Efficient Hybrid Solar Cells Based on Meso-Superstructured Organometal Halide Perovskites. *Science* **2012**, *338*, 643–647.

(13) Kim, H.-S.; Lee, C. R.; Im, J.-H.; Lee, K.-B.; Moehl, T.; Marchioro, A.; Moon, S.-J.; Humphry-Baker, R.; Yum, J.-H.; Moser, J. E. et al. Lead Iodide Perovskite Sensitized All-Solid-State Submicron Thin Film Mesoscopic Solar Cell with Efficiency Exceeding 9%. *Sci. Rep.* **2012**, *2*.

(14) Green, M. A.; Ho-Baillie, A.; Snaith, H. J. The emergence of perovskite solar cells. *Nat. Photonics* **2014**, *8*, 506–514.

(15) Stranks, S. D.; Snaith, H. J. Metal-halide perovskites for photovoltaic and light-emitting devices. *Nat. Nanotechnol.* **2015**, *10*, 391–402.

(16) Eperon, G. E.; Leijtens, T.; Bush, K. A.; Prasanna, R.; Green, T.; Wang, J. T.-W.; McMeekin, D. P.; Volonakis, G.; Milot, R. L.; May, R. et al. Perovskite-perovskite tandem photovoltaics with optimized band gaps. *Science* **2016**, *354*, 861–865.

(17) Jung, E. H.; Jeon, N. J.; Park, E. Y.; Moon, C. S.; Shin, T. J.; Yang, T.-Y.; Noh, J. H.; Seo, J. Efficient, stable and scalable perovskite solar cells using poly(3-hexylthiophene). *Nature* **2019**, *567*, 511–515.

(18) Best Research-Cell Efficiencies. `https://www.nrel.gov/pv/cell-efficiency.html` (accessed Feb. 12, 2019).

(19) Wang, R.; Mujahid, M.; Duan, Y.; Wang, Z.-K.; Xue, J.; Yang, Y. A Review of Perovskites Solar Cell Stability. *Adv. Funct. Mater.* **2019**, *29*, 1808843.

(20) Boyd, C. C.; Cheacharoen, R.; Leijtens, T.; McGehee, M. D. Understanding Degradation Mechanisms and Improving Stability of Perovskite Photovoltaics. *Chem. Rev.* **2019**, *119*, 3418–3451.

(21) Giustino, F.; Snaith, H. J. Toward Lead-Free Perovskite Solar Cells. *ACS Energy Lett.* **2016**, *1*, 1233–1240.

(22) De Angelis, F. The Prospect of Lead-Free Perovskite Photovoltaics. *ACS Energy Lett.* **2021**, *6*, 1586–1587.

(23) Slavney, A. H.; Hu, T.; Lindenberg, A. M.; Karunadasa, H. I. A Bismuth-Halide Double Perovskite with Long Carrier Recombination Lifetime for Photovoltaic Applications. *J. Am. Chem. Soc.* **2016**, *138*, 2138–2141.

(24) McClure, E. T.; Ball, M. R.; Windl, W.; Woodward, P. M. Cs_2AgBiX_6 (X = Br, Cl) - New Visible Light Absorbing, Lead-Free Halide Perovskite Semiconductors. *Chem. Mater.* **2016**, *28*, 1348–1354.

(25) Volonakis, G.; Filip, M. R.; Haghighirad, A. A.; Sakai, N.; Wenger, B.; Snaith, H. J.; Giustino, F. Lead-Free Halide Double Perovskites via Heterovalent Substitution of Noble Metals. *J. Phys. Chem. Lett.* **2016**, *7*, 1254–1259.

(26) Volonakis, G.; Haghighirad, A. A.; Milot, R. L.; Sio, W. H.; Filip, M. R.; Wenger, B.; Johnston, M. B.; Herz, L. M.; Snaith, H. J.; Giustino, F. $Cs_2InAgCl_6$: A New Lead-Free Halide Double Perovskite with Direct Band Gap. *J. Phys. Chem. Lett.* **2017**, *8*, 772–778.

(27) Volonakis, G.; Sakai, N.; Snaith, H. J.; Giustino, F. Oxide Analogs of Halide Perovskites and the New Semiconductor Ba_2AgIO_6. *J. Phys. Chem. Lett.* **2019**, *10*, 1722–1728.

(28) Tran, T. T.; Panella, J. R.; Chamorro, J. R.; Morey, J. R.; McQueen, T. M. Designing indirect–direct bandgap transitions in double perovskites. *Mater. Horiz.* **2017**, *4*, 688–693.

(29) Slavney, A. H.; Leppert, L.; Bartesaghi, D.; Gold-Parker, A.; Toney, M. F.; Savenije, T. J.; Neaton, J. B.; Karunadasa, H. I. Defect-Induced Band-Edge Reconstruction of a Bismuth-Halide Double Perovskite for Visible-Light Absorption. *J. Am. Chem. Soc.* **2017**, *139*, 5015–5018.

(30) Slavney, A. H.; Leppert, L.; Saldivar Valdes, A.; Bartesaghi, D.; Savenije, T. J.; Neaton, J. B.; Karunadasa, H. I. Small-Band-Gap Halide Double Perovskites. *Angew. Chem.* **2018**, *57*, 12765–12770.

(31) Wei, F.; Deng, Z.; Sun, S.; Hartono, N. T. P.; Seng, H. L.; Buonassisi, T.; Bristowe, P. D.; Cheetham, A. K. Enhanced visible light absorption for lead-free double perovskite $Cs_2AgSbBr_6$. *Chem. Commun.* **2019**, *55*, 3721–3724.

(32) Greul, E.; Petrus, M. L.; Binek, A.; Docampo, P.; Bein, T. Highly stable, phase pure $Cs_2AgBiBr_6$ double perovskite thin films for optoelectronic applications. *J. Mat. Chem. A* **2017**, *5*, 19972–19981.

(33) Luo, J.; Li, S.; Wu, H.; Zhou, Y.; Li, Y.; Liu, J.; Li, J.; Li, K.; Yi, F.; Niu, G. et al. $Cs_2AgInCl_6$ Double Perovskite Single Crystals: Parity Forbidden Transitions and Their Application For Sensitive and Fast UV Photodetectors. *ACS Photonics* **2017**, *5*, 398–405.

(34) Wu, C.; Du, B.; Luo, W.; Liu, Y.; Li, T.; Wang, D.; Guo, X.; Ting, H.; Fang, Z.; Wang, S. et al. Highly Efficient and Stable Self-Powered Ultraviolet and Deep-Blue Photodetector Based on $Cs_2AgBiBr_6/SnO_2$ Heterojunction. *Adv. Opt. Mater.* **2018**, *6*, 1800811.

(35) Gao, W.; Ran, C.; Xi, J.; Jiao, B.; Zhang, W.; Wu, M.; Hou, X.; Wu, Z. High-Quality $Cs_2AgBiBr_6$ Double Perovskite Film for Lead-Free Inverted Planar Heterojunction Solar Cells with 2.2% Efficiency. *Chem. Phys. Chem.* **2018**, *19*, 1696–1700.

(36) Igbari, F.; Wang, R.; Wang, Z.-K.; Ma, X.-J.; Wang, Q.; Wang, K.-L.; Zhang, Y.; Liao, L.-S.; Yang, Y. Composition Stoichiometry of $Cs_2AgBiBr_6$ Films for Highly Efficient Lead-Free Perovskite Solar Cells. *Nano Lett.* **2019**, *19*, 2066–2073.

(37) Longo, G.; Mahesh, S.; Buizza, L. R. V.; Wright, A. D.; Ramadan, A. J.; Abdi-Jalebi, M.; Nayak, P. K.; Herz, L. M.; Snaith, H. J. Understanding the Performance-

Limiting Factors of $Cs_2AgBiBr_6$ Double-Perovskite Solar Cells. *ACS Energy Lett.* **2020**, *5*, 2200–2207.

(38) Yang, X.; Wang, W.; Ran, R.; Zhou, W.; Shao, Z. Recent Advances in $Cs_2AgBiBr_6$-Based Halide Double Perovskites as Lead-Free and Inorganic Light Absorbers for Perovskite Solar Cells. *Energy Fuels* **2020**, *34*, 10513–10528.

(39) Kung, P.-K.; Li, M.-H.; Lin, P.-Y.; Jhang, J.-Y.; Pantaler, M.; Lupascu, D. C.; Grancini, G.; Chen, P. Lead-Free Double Perovskites for Perovskite Solar Cells. *Solar RRL* **2020**, *4*, 1900306.

(40) Pan, W.; Wu, H.; Luo, J.; Deng, Z.; Ge, C.; Chen, C.; Jiang, X.; Yin, W.-J.; Niu, G.; Zhu, L. et al. $Cs_2AgBiBr_6$ single-crystal X-ray detectors with a low detection limit. *Nat. Photonics* **2017**, *11*, 726–732.

(41) Zhou, L.; Xu, Y.-F.; Chen, B.-X.; Kuang, D.-B.; Su, C.-Y. Synthesis and Photocatalytic Application of Stable Lead-Free $Cs_2AgBiBr_6$ Perovskite Nanocrystals. *Small* **2018**, *14*, 1703762.

(42) Yang, B.; Hong, F.; Chen, J.; Tang, Y.; Yang, L.; Sang, Y.; Xia, X.; Guo, J.; He, H.; Yang, S. et al. Colloidal Synthesis and Charge-Carrier Dynamics of $Cs_2AgSb_{1-y}Bi_yX_6$ (X: Br, Cl; 0 <= y<=1) Double Perovskite Nanocrystals. *Angew. Chem.* **2019**, *58*, 2278–2283.

(43) Keshavarz, M.; Debroye, E.; Ottesen, M.; Martin, C.; Zhang, H.; Fron, E.; Küchler, R.; Steele, J. A.; Bremholm, M.; Van de Vondel, J. et al. Tuning the Structural and Optoelectronic Properties of $Cs_2AgBiBr_6$ Double-Perovskite Single Crystals through Alkali-Metal Substitution. *Adv. Mater.* **2020**, *32*, 2001878.

(44) Wu, C.; Zhang, Q.; Liu, Y.; Luo, W.; Guo, X.; Huang, Z.; Ting, H.; Sun, W.; Zhong, X.; Wei, S. et al. The Dawn of Lead-Free Perovskite Solar Cell: Highly Stable Double Perovskite $Cs_2AgBiBr_6$ Film. *Adv. Sci.* **2018**, *5*, 1700759.

(45) Yang, J.; Bao, C.; Ning, W.; Wu, B.; Ji, F.; Yan, Z.; Tao, Y.; Liu, J.-M.; Sum, T. C.; Bai, S. et al. Stable, High-Sensitivity and Fast-Response Photodetectors Based on Lead-Free $Cs_2AgBiBr_6$ Double Perovskite Films. *Adv. Opt. Mater.* **2019**, *7*, 1801732.

(46) Luo, J.; Wang, X.; Li, S.; Liu, J.; Guo, Y.; Niu, G.; Yao, L.; Fu, Y.; Gao, L.; Dong, Q. et al. Efficient and stable emission of warm-white light from lead-free halide double perovskites. *Nature* **2018**, *563*, 541–545.

(47) Zhou, J.; Xia, Z.; Molokeev, M. S.; Zhang, X.; Peng, D.; Liu, Q. Composition design, optical gap and stability investigations of lead-free halide double perovskite $Cs_2AgInCl_6$. *J. Mater. Chem. A* **2017**, *5*, 15031–15037.

(48) Li, S.; Luo, J.; Liu, J.; Tang, J. Self-Trapped Excitons in All-Inorganic Halide Perovskites: Fundamentals, Status, and Potential Applications. *J. Phys. Chem. Lett.* **2019**, *10*, 1999–2007.

(49) Locardi, F.; Sartori, E.; Buha, J.; Zito, J.; Prato, M.; Pinchetti, V.; Zaffalon, M. L.; Ferretti, M.; Brovelli, S.; Infante, I. et al. Emissive Bi-Doped Double Perovskite $Cs_2Ag_{1-x}Na_xInCl_6$ Nanocrystals. *ACS Energy Lett.* **2019**, *4*, 1976–1982.

(50) Liu, Y.; Jing, Y.; Zhao, J.; Liu, Q.; Xia, Z. Design Optimization of Lead-Free Perovskite $Cs_2AgInCl_6$:Bi Nanocrystals with 11.4% Photoluminescence Quantum Yield. *Chem. Mater.* **2019**, *31*, 3333–3339.

(51) Manna, D.; Das, T. K.; Yella, A. Tunable and Stable White Light Emission in Bi^{3+}-Alloyed $Cs_2AgInCl_6$ Double Perovskite Nanocrystals. *Chem. Mater.* **2019**, *31*, 10063–10070.

(52) Li, S.; Shi, Z.; Zhang, F.; Wang, L.; Ma, Z.; Wu, D.; Yang, D.; Chen, X.; Tian, Y.; Zhang, Y. et al. Ultrastable Lead-Free Double Perovskite Warm-White Light-Emitting Devices with a Lifetime above 1000 Hours. *ACS Appl. Mater. Interfaces* **2020**, *12*, 46330–46339.

(53) Schade, L.; Mahesh, S.; Volonakis, G.; Zacharias, M.; Wenger, B.; Schmidt, F.; Kesava, S. V.; Prabhakaran, D.; Abdi-Jalebi, M.; Lenz, M. et al. Crystallographic, Optical, and Electronic Properties of the $Cs_2AgBi_{1-x}In_xBr_6$ Double Perovskite: Understanding the Fundamental Photovoltaic Efficiency Challenges. *ACS Energy Lett.* **2021**, *6*, 1073–1081.

(54) Leppert, L.; Rangel, T.; Neaton, J. B. Towards predictive band gaps for halide perovskites: Lessons from one-shot and eigenvalue self-consistent *GW*. *Phys. Rev. Materials* **2019**, *3*, 103803.

(55) Giustino, F. Electron-phonon interactions from first principles. *Rev. Mod. Phys.* **2017**, *89*, 015003.

(56) Capaz, R. B.; Spataru, C. D.; Tangney, P.; Cohen, M. L.; Louie, S. G. Temperature Dependence of the Band Gap of Semiconducting Carbon Nanotubes. *Phys. Rev. Lett.* **2005**, *94*, 036801.

(57) Marini, A. *Ab Initio* Finite-Temperature Excitons. *Phys. Rev. Lett.* **2008**, *101*, 106405.

(58) Giustino, F.; Louie, S. G.; Cohen, M. L. Electron-Phonon Renormalization of the Direct Band Gap of Diamond. *Phys. Rev. Lett.* **2010**, *105*, 265501.

(59) Cannuccia, E.; Marini, A. Effect of the Quantum Zero-Point Atomic Motion on the Optical and Electronic Properties of Diamond and Trans-Polyacetylene. *Phys. Rev. Lett.* **2011**, *107*, 255501.

(60) Gonze, X.; Boulanger, P.; Côté, M. Theoretical approaches to the temperature and zero-point motion effects on the electronic band structure. *Ann. Phys.* **2011**, *523*, 168–178.

(61) Cannuccia, E.; Marini, A. Zero point motion effect on the electronic properties of diamond, trans-polyacetylene and polyethylene. *Eur. Phys. J. B* **2012**, *85*, 320.

(62) Poncé, S.; Antonius, G.; Boulanger, P.; Cannuccia, E.; Marini, A.; Côté, M.; Gonze, X. Verification of first-principles codes: Comparison of total energies, phonon frequencies, electron–phonon coupling and zero-point motion correction to the gap between ABINIT and QE/Yambo. *Comput. Mater. Sci.* **2014**, *83*, 341–348.

(63) Kawai, H.; Yamashita, K.; Cannuccia, E.; Marini, A. Electron-electron and electron-phonon correlation effects on the finite-temperature electronic and optical properties of zinc-blende GaN. *Phys. Rev. B* **2014**, *89*, 085202.

(64) Antonius, G.; Poncé, S.; Boulanger, P.; Côté, M.; Gonze, X. Many-Body Effects on the Zero-Point Renormalization of the Band Structure. *Phys. Rev. Lett.* **2014**, *112*, 215501.

(65) Poncé, S.; Antonius, G.; Gillet, Y.; Boulanger, P.; Laflamme Janssen, J.; Marini, A.; Côté, M.; Gonze, X. Temperature dependence of electronic eigenenergies in the adiabatic harmonic approximation. *Phys. Rev. B* **2014**, *90*, 214304.

(66) Monserrat, B.; Needs, R. J. Comparing electron-phonon coupling strength in diamond, silicon, and silicon carbide: First-principles study. *Phys. Rev. B* **2014**, *89*, 214304.

(67) Engel, E. A.; Monserrat, B.; Needs, R. J. Vibrational renormalisation of the electronic band gap in hexagonal and cubic ice. *J. Chem. Phys.* **2015**, *143*, 244708.

(68) Lloyd-Williams, J. H.; Monserrat, B. Lattice dynamics and electron-phonon coupling calculations using nondiagonal supercells. *Phys. Rev. B* **2015**, *92*, 184301.

(69) Patrick, C. E.; Jacobsen, K. W.; Thygesen, K. S. Anharmonic stabilization and band gap renormalization in the perovskite $CsSnI_3$. *Phys. Rev. B* **2015**, *92*, 201205.

(70) Poncé, S.; Gillet, Y.; Laflamme Janssen, J.; Marini, A.; Verstraete, M.; Gonze, X. Temperature dependence of the electronic structure of semiconductors and insulators. *J. Chem. Phys.* **2015**, *143*, 102813.

(71) Antonius, G.; Poncé, S.; Lantagne-Hurtubise, E.; Auclair, G.; Gonze, X.; Côté, M. Dynamical and anharmonic effects on the electron-phonon coupling and the zero-point renormalization of the electronic structure. *Phys. Rev. B* **2015**, *92*, 085137.

(72) Molina-Sánchez, A.; Palummo, M.; Marini, A.; Wirtz, L. Temperature-dependent excitonic effects in the optical properties of single-layer MoS_2. *Phys. Rev. B* **2016**, *93*, 155435.

(73) Monserrat, B. Vibrational averages along thermal lines. *Phys. Rev. B* **2016**, *93*, 014302.

(74) Monserrat, B. Correlation effects on electron-phonon coupling in semiconductors: Many-body theory along thermal lines. *Phys. Rev. B* **2016**, *93*, 100301.

(75) Nery, J. P.; Allen, P. B. Influence of Fröhlich polaron coupling on renormalized electron bands in polar semiconductors: Results for zinc-blende GaN. *Phys. Rev. B* **2016**, *94*, 115135.

(76) Saidi, W. A.; Poncé, S.; Monserrat, B. Temperature Dependence of the Energy Levels of Methylammonium Lead Iodide Perovskite from First-Principles. *J. Phys. Chem. Lett.* **2016**, *7*, 5247–5252.

(77) Allen, P. B.; Nery, J. P. Low-temperature semiconductor band-gap thermal shifts: T^4 shifts from ordinary acoustic and T^2 from piezoacoustic coupling. *Phys. Rev. B* **2017**, *95*, 035211.

(78) Karsai, F.; Engel, M.; Kresse, G.; Flage-Larsen, E. Electron-phonon coupling in semiconductors within the *GW* approximation. *New J. Phys.* **2018**, *20*, 123008.

(79) Manna, D.; Kangsabanik, J.; Das, T. K.; Das, D.; Alam, A.; Yella, A. Lattice Dynamics and Electron-Phonon Coupling in Lead-Free $Cs_2AgIn_{1-x}Bi_xCl_6$ Double Perovskite Nanocrystals. *J. Phys. Chem. Lett.* **2020**, *11*, 2113–2120.

(80) Lee, W.; Hong, S.; Kim, S. Colloidal Synthesis of Lead-Free Silver–Indium Double-Perovskite $Cs_2AgInCl_6$ Nanocrystals and Their Doping with Lanthanide Ions. *J. Phys. Chem. C* **2019**, *123*, 2665–2672.

(81) Liu, F.; Marongiu, D.; Pau, R.; Sarritzu, V.; Wang, Q.; Lai, S.; Lehmann, A. G.; Quochi, F.; Saba, M.; Mura, A. et al. Ag/In lead-free double perovskites. *EcoMat.* **2020**, *2*, e12017.

(82) Zacharias, M.; Giustino, F. One-shot calculation of temperature-dependent optical spectra and phonon-induced band-gap renormalization. *Phys. Rev. B* **2016**, *94*, 075125.

(83) Zacharias, M.; Giustino, F. Theory of the special displacement method for electronic structure calculations at finite temperature. *Phys. Rev. Research* **2020**, *2*, 013357.

(84) Hybertsen, M. S.; Louie, S. G. Electron correlation in semiconductors and insulators: Band gaps and quasiparticle energies. *Phys. Rev. B* **1986**, *34*, 5390–5413.

(85) Hedin, L. New Method for Calculating the One-Particle Green's Function with Application to the Electron-Gas Problem. *Phys. Rev.* **1965**, *139*, A796–A823.

(86) Aryasetiawan, F.; Gunnarsson, O. The *GW* method. *Rep. Prog. Phys.* **1998**, *61*, 237–312.

(87) Golze, D.; Dvorak, M.; Rinke, P. The *GW* Compendium: A Practical Guide to Theoretical Photoemission Spectroscopy. *Front. Chem.* **2019**, *7*.

(88) Rinke, P.; Qteish, A.; Neugebauer, J.; Freysoldt, C.; Scheffler, M. Combining *GW* calculations with exact-exchange density-functional theory: an analysis of valence-band photoemission for compound semiconductors. *New J. Phys.* **2005**, *7*, 126.

(89) Fuchs, F.; Furthmüller, J.; Bechstedt, F.; Shishkin, M.; Kresse, G. Quasiparticle band structure based on a generalized Kohn-Sham scheme. *Phys. Rev. B* **2007**, *76*, 115109.

(90) Rinke, P.; Qteish, A.; Neugebauer, J.; Scheffler, M. Exciting prospects for solids: Exact-exchange based functionals meet quasiparticle energy calculations. *Phys. Status Solidi B* **2008**, *245*, 929–945.

(91) Jiang, H.; Gomez-Abal, R. I.; Rinke, P.; Scheffler, M. First-principles modeling of localized d states with the GW@LDA + U approach. *Phys. Rev. B* **2010**, *82*, 045108.

(92) Waroquiers, D.; Lherbier, A.; Miglio, A.; Stankovski, M.; Poncé, S.; Oliveira, M. J. T.; Giantomassi, M.; Rignanese, G.-M.; Gonze, X. Band widths and gaps from the Tran-Blaha functional: Comparison with many-body perturbation theory. *Phys. Rev. B* **2013**, *87*, 075121.

(93) van Setten, M. J.; Giantomassi, M.; Gonze, X.; Rignanese, G.-M.; Hautier, G. Automation methodologies and large-scale validation for GW: Towards high-throughput GW calculations. *Phys. Rev. B* **2017**, *96*, 155207.

(94) Blase, X.; Attaccalite, C.; Olevano, V. First-principles GW calculations for fullerenes, porphyrins, phtalocyanine, and other molecules of interest for organic photovoltaic applications. *Phys. Rev. B* **2011**, *83*, 115103.

(95) Faber, C.; Attaccalite, C.; Olevano, V.; Runge, E.; Blase, X. First-principles GW calculations for DNA and RNA nucleobases. *Phys. Rev. B* **2011**, *83*, 115123.

(96) Blase, X.; Attaccalite, C. Charge-transfer excitations in molecular donor-acceptor complexes within the many-body Bethe-Salpeter approach. *Appl. Phys. Lett.* **2011**, *99*, 171909.

(97) Marom, N.; Caruso, F.; Ren, X.; Hofmann, O. T.; Körzdörfer, T.; Chelikowsky, J. R.; Rubio, A.; Scheffler, M.; Rinke, P. Benchmark of GW methods for azabenzenes. *Phys. Rev. B* **2012**, *86*, 245127.

(98) Wilhelm, J.; Ben, M. D.; Hutter, J. *GW* in the Gaussian and Plane Waves Scheme with Application to Linear Acenes. *J. Chem. Theory Comput.* **2016**, *12*, 3623–3635.

(99) Shishkin, M.; Kresse, G. Self-consistent *GW* calculations for semiconductors and insulators. *Phys. Rev. B* **2007**, *75*, 235102.

(100) Filip, M. R.; Giustino, F. *GW*-quasiparticle band gap of the hybrid organic-inorganic perovskite $CH_3NH_3PbI_3$: Effect of spin-orbit interaction, semicore electrons, and self-consistency. *Phys. Rev. B* **2014**, *90*, 245145.

(101) Poncé, S.; Schlipf, M.; Giustino, F. Origin of Low Carrier Mobilities in Halide Perovskites. *ACS Energy Lett.* **2019**, *4*, 456–463.

(102) Heyd, J.; Scuseria, G. E.; Ernzerhof, M. Hybrid functionals based on a screened Coulomb potential. *J. Chem. Phys.* **2003**, *118*, 8207–8215.

(103) Brothers, E. N.; Izmaylov, A. F.; Normand, J. O.; Barone, V.; Scuseria, G. E. Accurate solid-state band gaps via screened hybrid electronic structure calculations. *J. Chem. Phys.* **2008**, *129*, 011102.

(104) Marzari, N.; Vanderbilt, D. Maximally localized generalized Wannier functions for composite energy bands. *Phys. Rev. B* **1997**, *56*, 12847.

(105) Souza, I.; Marzari, N.; Vanderbilt, D. Maximally localized Wannier functions for entangled energy bands. *Phys. Rev. B* **2001**, *65*, 035109.

(106) Marzari, N.; Mostofi, A. A.; Yates, J. R.; Souza, I.; Vanderbilt, D. Maximally localized Wannier functions: Theory and applications. *Rev. Mod. Phys.* **2012**, *84*, 1419.

(107) Biswas, T.; Ravindra, P.; Athresh, E.; Ranjan, R.; Avasthi, S.; Jain, M. Optical Properties of $Zn_2Mo_3O_8$: Combination of Theoretical and Experimental Study. *J. Phys. Chem. C* **2017**, *121*, 24766–24773.

(108) Zhang, X.-W.; Wang, E.-G.; Li, X.-Z. *Ab initio* investigation on the experimental observation of metallic hydrogen. *Phys. Rev. B* **2018**, *98*, 134110.

(109) Kang, Y.; Peelaers, H.; Krishnaswamy, K.; Van de Walle, C. G. First-principles study of direct and indirect optical absorption in $BaSnO_3$. *Appl. Phys. Lett* **2018**, *112*, 062106.

(110) Karsai, F.; Humer, M.; Flage-Larsen, E.; Blaha, P.; Kresse, G. Effects of electron-phonon coupling on absorption spectrum: K edge of hexagonal boron nitride. *Phys. Rev. B* **2018**, *98*, 235205.

(111) Huang, T. A.; Zacharias, M.; Lewis, D. K.; Giustino, F.; Sharifzadeh, S. Exciton–Phonon Interactions in Monolayer Germanium Selenide from First Principles. *J. Phys. Chem. Lett.* **2021**, *12*, 3802–3808.

(112) Baroni, S.; de Gironcoli, S.; Dal Corso, A.; Giannozzi, P. Phonons and related crystal properties from density-functional perturbation theory. *Rev. Mod. Phys.* **2001**, *73*, 515–562.

(113) Popescu, V.; Zunger, A. Extracting E versus $\mathbf{k}$ effective band structure from supercell calculations on alloys and impurities. *Phys. Rev. B* **2012**, *85*, 085201.

(114) Allen, P. B.; Heine, V. Theory of the temperature dependence of electronic band structures. *J. Phys. C: Solid State Phys.* **1976**, *9*, 2305–2312.

(115) Lihm, J.-M.; Park, C.-H. Phonon-induced renormalization of electron wave functions. *Phys. Rev. B* **2020**, *101*, 121102.

(116) Giannozzi, P.; Andreussi, O.; Brumme, T.; Bunau, O.; Nardelli, M. B.; Calandra, M.; Car, R.; Cavazzoni, C.; Ceresoli, D.; Cococcioni, M. et al. Advanced capabilities for materials modelling with Quantum ESPRESSO. *J. Phys. Condens. Matter* **2017**, *29*, 465901.

(117) Hohenberg, P.; Kohn, W. Inhomogeneous Electron Gas. *Phys. Rev.* **1964**, *136*, B864–B871.

(118) Perdew, J. P.; Burke, K.; Ernzerhof, M. Generalized Gradient Approximation Made Simple. *Phys. Rev. Lett.* **1996**, *77*, 3865–3868.

(119) Csonka, G. I.; Perdew, J. P.; Ruzsinszky, A.; Philipsen, P. H. T.; Lebègue, S.; Paier, J.; Vydrov, O. A.; Ángyán, J. G. Assessing the performance of recent density functionals for bulk solids. *Phys. Rev. B* **2009**, *79*, 155107.

(120) Hamann, D. R. Optimized norm-conserving Vanderbilt pseudopotentials. *Phys. Rev. B* **2013**, *88*, 085117.

(121) van Setten, M.; Giantomassi, M.; Bousquet, E.; Verstraete, M.; Hamann, D.; Gonze, X.; Rignanese, G.-M. The PseudoDojo: Training and grading a 85 element optimized norm-conserving pseudopotential table. *Comput. Phys. Commun.* **2018**, *226*, 39–54.

(122) Marini, A.; Hogan, C.; Grüning, M.; Varsano, D. yambo: An *ab initio* tool for excited state calculations. *Comput. Phys. Commun.* **2009**, *180*, 1392–1403.

(123) Sangalli, D.; Ferretti, A.; Miranda, H.; Attaccalite, C.; Marri, I.; Cannuccia, E.; Melo, P.; Marsili, M.; Paleari, F.; Marrazzo, A. et al. Many-body perturbation theory calculations using the yambo code. *J. Phys.: Condens. Matter* **2019**, *31*, 325902.

(124) Godby, R. W.; Needs, R. J. Metal-insulator transition in Kohn-Sham theory and quasiparticle theory. *Phys. Rev. Lett.* **1989**, *62*, 1169–1172.

(125) Li, T.; Zhao, X.; Yang, D.; Du, M.-H.; Zhang, L. Intrinsic Defect Properties in Halide Double Perovskites for Optoelectronic Applications. *Phys. Rev. Appl.* **2018**, *10*, 041001.

(126) Lin, L. Adaptively Compressed Exchange Operator. *J. Chem. Theory Comput.* **2016**, *12*, 2242–2249.

(127) Mostofi, A. A.; Yates, J. R.; Lee, Y.-S.; Souza, I.; Vanderbilt, D.; Marzari, N. wannier90: A tool for obtaining maximally-localised Wannier functions. *Comput. Phys. Commun.* **2008**, *178*, 685–699.

(128) Mostofi, A. A.; Yates, J. R.; Pizzi, G.; Lee, Y.-S.; Souza, I.; Vanderbilt, D.; Marzari, N. An updated version of wannier90: A tool for obtaining maximally-localised Wannier functions. *Comput. Phys. Commun.* **2014**, *185*, 2309–2310.

(129) Pizzi, G.; Vitale, V.; Arita, R.; Blügel, S.; Freimuth, F.; Géranton, G.; Gibertini, M.; Gresch, D.; Johnson, C.; Koretsune, T. et al. Wannier90 as a community code: new features and applications. *J. Phys. Condens. Matter.* **2020**, *32*, 165902.

(130) Poncé, S.; Margine, E.; Verdi, C.; Giustino, F. EPW: Electron–phonon coupling, transport and superconducting properties using maximally localized Wannier functions. *Comput. Phys. Commun.* **2016**, *209*, 116–133.

(131) Rohlfing, M.; Krüger, P.; Pollmann, J. Quasiparticle Band Structure of CdS. *Phys. Rev. Lett.* **1995**, *75*, 3489–3492.

(132) Umari, P.; Fabris, S. Importance of semicore states in GW calculations for simulating accurately the photoemission spectra of metal phthalocyanine molecules. *J. Chem. Phys.* **2012**, *136*, 174310.

(133) Filip, M. R.; Patrick, C. E.; Giustino, F. GW quasiparticle band structures of stibnite, antimonselite, bismuthinite, and guanajuatite. *Phys. Rev. B* **2013**, *87*, 205125.

(134) Filip, M. R.; Verdi, C.; Giustino, F. GW Band Structures and Carrier Effective Masses of $CH_3NH_3PbI_3$ and Hypothetical Perovskites of the Type $APbI_3$: A = NH_4, PH_4, AsH_4, and SbH_4. *J. Phys. Chem. C* **2015**, *119*, 25209–25219.

(135) Leveillee, J.; Volonakis, G.; Giustino, F. Phonon-Limited Mobility and Electron–Phonon Coupling in Lead-Free Halide Double Perovskites. *J. Phys. Chem. Lett.* **2021**, *12*, 4474–4482.

(136) Schlipf, M.; Poncé, S.; Giustino, F. Carrier Lifetimes and Polaronic Mass Enhancement in the Hybrid Halide Perovskite $CH_3NH_3PbI_3$ from Multiphonon Fröhlich Coupling. *Phys. Rev. Lett.* **2018**, *121*, 086402.

(137) Sio, W. H.; Verdi, C.; Poncé, S.; Giustino, F. *Ab initio* theory of polarons: Formalism and applications. *Phys. Rev. B* **2019**, *99*, 235139.

(138) Devreese, J. T.; Alexandrov, A. S. Fröhlich polaron and bipolaron: recent developments. *Rep. Prog. Phys.* **2009**, *72*, 066501.

(139) Schultz, T. D. Slow Electrons in Polar Crystals: Self-Energy, Mass, and Mobility. *Phys. Rev.* **1959**, *116*, 526–543.